Static and dynamic behaviours of a self-expanding nitinol stent real contact area within a PTFE catheter: a multiscale approach

Achref Sallami^{a,b}, Pierrick Malecot^{d,e}, Fabrice Richard^a, Michaël Fontaine^c, Arnaud Lejeune^a, Sébastien David^b, Paul Vescovo^b, Christophe Moureaux^b, Philippe Stempflé^{c,*}

^aUniversité de Franche-Comté, CNRS, institut FEMTO-ST, F-25000 Besançon, France ^bCisteo MEDICAL, 1 rue Anne de Pardieu, F-25000 Besançon, France ^cSUPMICROTECH, CNRS, institut FEMTO-ST, F-25000 Besançon, France ^dUniversité de Bretagne Sud, CNRS, IRDL, F-56100 Lorient, France ^eAcadémie militaire de Saint-Cyr Coëtquidan, CReC Saint-Cyr, F-56380 Guer, France

Abstract

Current research on self-expanding super-elastic nitinol stents is mainly focused on designing geometries suited to the human venous and arterial systems. This study specifically considers a patented one-piece double cross-sectional stent designed to address venous stenosis affecting the vena cava, iliac veins, and their bifurcations. During its release, numerous tribological challenges arise as the stent slides along the guide-wire (so-called catheter). These are mainly connected to the lack of knowledge related to (i) its frictional behaviour and (ii) the level of contact pressure linked to the unknown real contact area between the compressed stent and the polytetrafluoroethylene (PTFE) catheter.

This paper describes an original multi-scale approach allowing to determine the contact pressure, the evolutions of the real contact area and the shear stresses at the interface during the stent release. A topographical optimization criterion will be finally provided enabling to control both friction and stick-slip phenomena at the stent catheter interface.

Keywords: Self-expanding nitinol stent, Frictional behaviour law, X-ray tomography, topographical analysis, Persson's contact theory

Email addresses: asallami@cisteomedical.com (Achref Sallami), pierrick.malecot@st-cyr.terre-net.defense.gouv.fr (Pierrick Malecot), fabrice.richard@univ-fcomte.fr (Fabrice Richard), michael.fontaine@ens2m.fr (Michaël Fontaine), arnaud.lejeune@univ-fcomte.fr (Arnaud Lejeune), sdavid@cisteomedical.com (Sébastien David), pvescovo@cisteomedical.com (Paul Vescovo), cmoureaux@cisteomedical.com (Christophe Moureaux), philippe.stempfle@ens2m.fr (Philippe Stempflé)

^{*}Corresponding author

1. Introduction

Ni-Ti alloys - so-called nitinol [1]- are the most well-known shape memory alloys (SMAs) [2]. They have the ability to recover their original shapes even after a significant externally applied loads owing to a solid-to-solid reversible phase transformation. Nitinol exhibits two important behaviours: (i) a shape memory effect (SME) [3] in which thermal effect activates the reverse phase transformation, and (ii) a super-elastic behaviour (SE) [4] which is only activated by mechanically loading and unloading the structure. For a same alloy composition, the nitinol behaviour i.e, SME or SE - is mainly dependent on the chosen heat treatment [5]. Its versatility leads nitinol to be an interesting candidate for various applications ranking from mechanical engineering to medicine [6, 7]. Round orthodontic bows, endodontic rotary files and stents represent the main medical applications of nitinol [8, 9, 10]. Considering the treatment of arterial or venous stenosis, all implanted nitinol stents displays 12 SE behaviour after a suitable heat treatment being applied [11]. During large deformations, nitinol stent is subjected to an isothermal reversible phase transformation from austenite to martensite, which induces this SE behaviour. Owing to the metastability of the martensite, the alloy returns to the austenitic state as soon as the stress is released involving, in turn, the initial shape regains [12, 13, 14], as shown in Fig. 1.

The present work focuses on an original one-piece double cross-sectional stent (Fig. 2) used 18 in the treatment of venous stenosis, affecting the vena cava, iliac veins and their bifurcations. As shown in Fig 2b, the stent is actually constituted of two parts with different diameters connected 20 together and dedicated to respectively the illiac vein for the Leg part ($\phi^{Leg} = 12$ mm) and the vena cava for the *Body* part ($\phi^{Body} = 24$ mm), as illustrated in Fig. 2a. Besides, SE nitinol stents are placed in veins by catheterization [15]. For this purpose, polytetrafluoroethylene (PTFE) is commonly used as catheter main material, owing to its low friction and good bio-compatibility. Because a stent is a large object, its section must be reduced into a wire form to be inserted in martensitic structure within the PTFE catheter. Once positioned in the diseased vein, it returns to its shape on its own (in austenitic structure, Fig. 2c) taking advantage of the SE behaviour to expand the diseased vein [16], without any use of balloon as needed for stainless steel stents.

The aim of this paper is to enhance our knowledge about the release force, which is strongly 29 dependent on the tribological behaviour and the shear stress at the interface of the nitinol stent

and the PTFE catheter. In section 3.1, the evaluation of the static real contact area induced by the compressed stent within the PTFE catheter will be investigated by combining X-ray tomography and topographical analysis using the Persson's contact theory [17]. The real contact area dynamics 33 will be then evaluated, in section 3.2, by integrating both, (i) the materials part of the friction dissipation and the effect of the stent topography by applying a multi-scale approach combining topographical analysis, tribological behaviours of nitinol stent and nitinol tube rubbing within a 36 PTFE catheter and, (ii) the linear part of Persson's curve. Finally, the evolution of the tangential 37 stress at the interface between the stent and the PTFE catheter will be computed in traction and compression at various velocities, in section 3.3. Since this tangential stress integrates both the stent design and the materials behaviours, it will be likely to simplify the numerical model which 40 allows to compute the releasing force depending on the stent design.

2. Materials and methods

2.1. Tribological setup 43

47

51

57

- In order to simulate the stent release, two samples have been forced to rub within a PTFE 44 catheter (inner diameter $\phi_{ID} = 5$ mm, outer diameter $\phi_{OD} = 6$ mm, wall thickness $w_t = 0.5$ mm) by 45 means of a tensile testing machine (Instron Electropuls E 10000), as shown in Fig. 3 and 4a: 46
- The first one is a laser-cut stent machined from an ASTM F-2063 bio-medical nitinol displaying a suitable design for the aforementioned medical application. The stent is a one-48 piece double cross-sectional of respectively 24 mm - for the Body part - and 12 mm - for the Leg part – with a stent strand width around 180 µm, as shown in Fig. 2b. It has been thermally treated in order to optimize the SE behaviour, as reported in our previous work [11]. As shown in Fig. 3, once compressed, the diameters of each part decrease to the in-52 ternal diameter of the catheter (i.e., 5 mm), generating in return, an average normal contact pressure $\overline{\sigma_0}$. The latter is imposed by radial compression of each part of the stent within the PTFE catheter, owing to the SE behaviour of nitinol connected to phase changes from 55 austenite to martensite (Fig. 1). Evaluation of $\overline{\sigma_0}$ will be detailed in section 3.1.2. However, 56 it is worth mentioning that variations of this average normal contact pressure $\overline{\sigma_0}$ – taking into account both the Leg and Body contributions – are likely to be expected in dynamics, as 58

the main driving force controlling the frictional behaviour during the stent release. Indeed, pulling or pushing forces are directly connected to tangential forces induced by traction or compression of nitinol stent within the PTFE catheter. Thus, in these configurations, the friction component not only includes material part but also the geometrical one imposed by the double section of the stent. Hence, the tangential force F_T has been quantified by a load cell of the tensile testing machine during pulling and pushing tests for various velocities - i.e., 100, 500, and 1000 μ m.s⁻¹, respectively and for a maximum displacement of 10 mm.

• The second one is a smoothed tube ($R_q = 216.7 \pm 29.8$ nm) of ASTM F-2063 bio-medical nitinol (inner diameter $\phi_{ID} = 4.1$ mm, outer diameter $\phi_{OD} = 5.0$ mm, wall thickness $w_t = 0.45$ mm). It has been used to dissociate the material part of friction component from the geometrical one (i.e., the design). Indeed, as shown in Fig. 4b, an accurate normal pressure has been here applied on the nitinol/PTFE assembly with a torque screw controlled by a strain gauge glued on the clamping ring, in order to extract the friction coefficients of the nitinol/PTFE couple without any influence of the design. Tensile test provides the evolution of the pulling/pushing forces as a function of the displacement, for various normal loads assessed by the strain gauge. Velocities are the same as for the previous tests but three clamping forces F_N have been imposed for each velocity – i.e., 7.4, 8.2, and 14.1 N, respectively. Friction coefficients have been finally computed by dividing the tangential forces F_T to the normal loads F_N , for each velocity. Since the tube is really smooth, the resulting friction coefficient can be then attributed to only the pair of materials in contact.

All tests have been carried out at room temperature and ambient environment. The capacity of the machine is \pm 1000 N on loading. Materials properties are compiled in Table 1 [11].

81 2.2. X-ray Tomography

X-ray micro nano tomographic equipment (RX-solution Easytom) has been used to determine the aforementioned average normal contact pressure $\overline{\sigma_0}$ imposed by the compressed stent on the PTFE catheter, as shown in Fig. 5a. For this purpose, a parallel beam of monochromatic X-rays and a single 2D detector are used (tube voltage and current are 116 keV and 102 μ A, respectively). The stent/catheter assembly is rotated to acquire the different projections needed for tomographic reconstruction (Fig. 5b). Projection were taken every 0.3° for a total sample rotation of 360° (corresponding to 1200 projections per scan). Image analysis has been done with VGSTUDIO MAX software using a Filtered Back-projection algorithm based on grey level thresholds for image reconstruction [18]. Determination of the average normal contact pressure $\overline{\sigma}_0$ from X-ray tomography data will be detailed in section 3.1.2.

2.3. Topographical analysis

Measurements have been carried out with an InfiniteFocus topo-microscope from the Austrian company Alicona (Fig. 6). The sample (i.e., stent/tube assembly in Fig. 6a) is placed on the motorized stage and illuminated by modulated lightening. Using a beam splitting mirror, white light is inserted into the optical path of the system and focused onto the sample threw the objective. During the analysis, the distance between the objective and the sample is gradually changed so that the point-to-point contrast variation can be computed. From a series of partially focused images that are automatically acquired, the system reconstructs a 3D images of the sample, where each pixel is at the maximum focus (see Fig. 6b). The vertical and lateral resolution is defined by the choice of the objective (between $\times 5$ and $\times 100$). Lateral measurement accuracy of 400 nm and vertical of 10 nm can be achieved. The maximal slope angle Δ_q which could be assessed is about 87° [19]. Post-processing has been carried out using Gwyddion software [20, 21].

4 3. Results and discussion

3.1. Evaluation of the static real contact area occurring within PTFE catheter

The static real contact area generated by radial compression of the stent within the PTFE catheter can be computed using the Persson's contact theory [17, 27] by means of Eq. 1, involving the mechanical parameter E', the scale dependent topographical $\overline{\Delta_q}(\zeta)$ properties, and the average contact pressure $\overline{\sigma_0}$ imposed by the stent within the catheter:

$$\frac{A_r(\zeta)}{A_0} = erf(\frac{\overline{\sigma_0}}{E'\overline{\Delta_a}(\zeta)}) \tag{1}$$

with erf is the Gaussian error function, $A_r(\zeta)$ and A_0 being the real and nominal contact area, respectively. ζ is a magnification parameter – i.e., the number of scale components used to described the surface roughness – and E' is the effective elastic modulus, defined as follows:

$$\frac{1}{E'} = \frac{1 - v_{PTFE}^2}{E_{PTFE}} + \frac{1 - v_{Nitinol}^2}{E_{Nitinol}} \tag{2}$$

with v_{α} and E_{α} , the Poisson's ratio and the Young's modulus of PTFE and martensitic phase of nitinol, respectively.

Referring to the properties compiled in Table 1, the effective elastic modulus E' is then evaluated from Eq. 2 to 1452 MPa. The static real contact area needs two steps to be determined as detailed in the following.

3.1.1. Evaluation of the average root mean square asperity slope $\overline{\Delta_q}(\zeta)$

The average root mean square asperity slope $\overline{\Delta_q}(\zeta)$ can accurately be evaluated using optical topographical analysis as long as the catheter is transparent enough to avoid light scattering that inevitably leads to measurement artefacts. Since the PTFE catheter does not have these optical properties, a glass tube displaying the same inner diameter has been used instead (Fig. 6a). Indeed, the average asperity slope $\overline{\Delta_q}(\zeta)$ of stent topography is not greatly affected by the material change from PTFE to glass because the PTFE catheter, owing to its softness, originally takes the form imposed by the compressed stent within its inner volume. As a result, Fig. 6b shows a typical 3D topographical view of the stent compressed within a glass tube, revealing the different stent strands without any artefact.

- From a typical 3D topographical map of the stent within the glass tube (Fig 7a) a representative enlargement is then obtained in order to first define the nominal contact area A_0 (see Fig. 7b) using Gwyddion software [20]. The smallest length of the rectangle (i.e., 180 μ m) is here chosen to be the same as the stent's strand width, which is the largest possible length, as suggested by Persson [17], in this discontinuous contact case. A typical representative nominal contact area A_0 is thus illustrated in Fig. 7b.
- Secondly, the average root mean square slope Δq(ζ) is then computed with Gwyddion by extracting an average profile on A₀ in the direction of sliding (Fig. 7b), as plotted in Fig. 7c
 [22]. The latter is actually averaged on sixty individual profiles for statistical validity. Since Δq(ζ) is scale dependent, its value has been computed for the highest magnification i.e.,

 $\zeta = \frac{q_1}{q_0} \simeq 39$ – suited by the topographical image resolution [22, 23], with q_1 and q_0 , the maximum and minimum cut-off frequencies corresponding to the short wavelength cut-off and the long wavelength roll-off, respectively [17]. It is worth mentioning that some authors prefer to use q_L – involving the lateral size of the surface area L – instead of q_0 , in that case our $\zeta = \frac{q_1}{q_L} \simeq 64$ instead of 39.

• Finally, the average root mean square asperity slope $\overline{\Delta_q}$, computed on eleven measurements (cf. Fig. 7b), is then evaluated at 0.9702 ± 0.032 .

Figure 8 shows the evolution of the contact area ratio $\frac{A_r}{A_0}$ versus the contact pressure σ_0 , following Eq. 1. As expected, the Persson's contact theory provides the evolution of the real contact from zero to full contact – i.e., when $A_r = A_0$:

- In the first part (red dotted line in Fig. 8a), the real contact area is proportional to the applied pressure σ_0 , in agreement with other theories proposed by Greenwood and Williamson [24] and, Bush, Gibson and Thomas [25], for instance.
- In the second part (blue curve in Fig. 8a), the real contact area is no longer proportional to the contact pressure σ_0 . The latter is specific to the Persson's contact theory [17], as it well characterizes the contact behaviour of soft polymers submitted to high loadings [26]. It is worth mentioning here that Persson's contact theory actually encompasses the linear and non-linear cases as a generalized relationship (Eq. 1) [27].

In order to extract from this curve the average actual contact area ratio $\frac{\overline{A_r}}{A_0}$ generated by the stent within the PTFE catheter, the average actual contact pressure $\overline{\sigma_0}$ induced by the stent into the catheter needs to be determined as a second stage.

3.1.2. Evaluation of the average contact pressure $\overline{\sigma_0}$

142

143

145

146

147

151

152

154

155

156

158

162

The average contact pressure $\overline{\sigma_0}$ generated by the nitinol stent compression within the PTFE catheter can be evaluated by combining X-ray tomography assessment (Fig. 9c-d) with the well-known elastic coupling relationship (Eq. 3) [28] associated with the sketch illustrating the double cross-sectional stent compressed within the catheter (Fig. 9a-b). Parameters of Eq. 3 are reported in Fig. 9e.

$$\Delta D = \frac{\sigma_0 D^2}{2w_t E_{PTFE}} \tag{3}$$

This can be accurately carried out by X-ray tomography because the nitinol stent can be easily distinguished from the PTFE catheter thanks to their different densities ($\rho_{Nitinol} = 6.45 \text{ g/cm}^3$ and $\rho_{PTFE} = 2.2 \text{ g/cm}^3$), as shown in Fig. 9c. Thus, by measuring the deformation of the inner diameter $\Delta D_{i=\{1-4\}}$ at different locations in the PTFE catheter with the tomography software (Fig. 9b and d), the average contact pressure $\overline{\sigma_0}$ including the influence of each part of the stent – i.e., Leg and Body – can be computed using Eq. 4:

174

175

182

183

184

185

191

$$\overline{\sigma_0} = \frac{2w_t E_{PTFE}}{D^2} \overline{\Delta D} \tag{4}$$

The average contact pressure $\overline{\sigma_0}$ is finally evaluated at 18.9 \pm 2.1 MPa, considering the dimensions compiled in table 2.

Inserting this value into Eq. 1, an average contact area ratio of 1.5 ± 0.16 % is obtained, as plotted in Fig. 8b. Insert Fig. 8c finally plots a typical view of this average real contact area obtained after a vertical slicing, consisting of decreasing a binarization threshold on the stent's strands topographical view to have a discrete area of 1.5%.

The actual contact area finally appears discrete with small contact spots (Fig. 8c). This peculiarity will be likely to influence the tribological behaviour of the stent within the catheter - by means of the tangential stress at the interface between the stent and the PTFE catheter - as discussed in section 3.3.

However, it is worth noting that this real contact area value clearly depends on the stent design. Indeed, Fig. 10a confirms this assumption by plotting, for instance, the evolution of the real contact areas for two stent geometries. Assuming a same average contact pressure $\overline{\sigma_0}$, their specific design clearly leads to different contact area ratios (Fig. 10b): i.e., $1.5 \pm 0.16 \%$ (A) versus 2.25 $\pm 0.23 \%$ (B), which in turn, obviously leads to a specific shear stress at the interface.

Let us observe the dynamical behaviour of the real contact area when the stent is rubbing within the catheter.

3.2. Real contact area dynamics during stent sliding within PTFE catheter

3.2.1. Tribological behaviour of nitinol stent within PTFE catheter

Figures 11a and b show the evolution of the pulling (Fig. 11a) and pushing (Fig. 11b) force versus displacement assessed when the nitinol stent is rubbing within the PTFE catheter for three velocities. Frictional behaviours appear to be really noisy owing to a stick-slip-like behaviour. As well known [26, 29], stick-slip arises from interplay of friction with dynamic of mechanical system. According to Mate [29], there are no less than three possible sources of stick-slip, which are: (i) the velocity-controlled stick slip; (ii) the time-controlled stick-slip and (iii) the displacement-controlled stick-slip. All these mechanisms can obviously interfere independently or simultaneously depending on the scale being considered. In order to identify the main source of stick-slip occurring for our stent-catheter system, all these mechanisms are going to be further analysed:

- First, the *velocity-controlled stick-slip* mostly occurs when both (i) the static friction coefficient (μ_s) is greater that the kinetic one (μ_k) and, (ii) when the latter continuously decreases with the sliding velocity (in logarithmic scale following a certain slope). It is worth noting that this is only licit for small range of friction versus the velocity curve. Thus, when the energy supplied by friction becomes greater than the dissipated energy within the contact, the extra energy then drives stick-slip oscillations. The latter are generally observed for high loads and low slope value. By considering simultaneously, (i) the evolution of the tangential force with the sliding distance (Fig. 11) for all velocities and, (ii) the average values of the friction force as a function of the sliding velocity reported in Table 3, none of the conditions satisfying this type of stick-slip mechanism can be observed. Hence, velocity is clearly not the factor controlling the stick-slip occurrence observed in Fig 11.
- Second, considering the *time-controlled stick-slip*, the static friction force is now supposed to increase with the stick time in contrast to what is observed in the previous case. That means that the static friction leads to rise the longer the two surfaces are in stationary contact. Hence, this stick-slip mechanism is likely to supplant the previous one whether the increase in static friction during the sticking phase is greater to the variation of the kinetic friction during the slip phase. Of course, this kind of mechanism can only be observed at

very low sliding speeds allowing time for the adhesion forces to establish themselves. Hence this stick-slip component can clearly be neglected here, owing to the sliding velocities range being considered compared to the viscoelastic characteristic time of PTFE.

• At last, stick-slip occurrence can be also caused by a friction force varying as a function of the position over the sliding surface – i.e., the *displacement-controlled stick-slip*. This is generally observed on non-uniform surface as met for the stent, where topography and design can influence the average contact pressure during sliding.

Hence, stick-slip-like behaviours observed in Fig. 11 can be considered to be induced by the evolution of the aforementioned discrete real contact area, itself connected to the variation of the average contact pressure with time, $\overline{\sigma_0}(t)$, or sliding distance, $\overline{\sigma_0}(d)$. This assumption is reinforced by the fact that fluctuation amplitudes of tangential force (Fig. 11) are clearly reduced during compression (Fig. 11b) compared to the ones in traction (Fig. 11a). Thus, this unstable behaviour of the friction force can also be attributed to the stent mesh design, whose variations of local geometry are likely to evolve during the sliding distance.

Once again, any modification in stent design should lead to change its tribological behaviour within catheter, by means of the real contact area ratio, which changes the contact stiffness. In order to ascertain how the actual contact area really evolves during the sliding process, the Persson's contact theory is still going to be employed in the following section, but in a dynamic manner.

3.2.2. Evolution of the real contact area vs. sliding distance

Whenever the contact area ratio $\frac{A_r}{A_0}$ versus contact pressure stays confined in the linear part of the Persson's curves (Fig. 8a, for instance), the Persson's relationship (Eq. 1) can be simplified by expanding the error function to the first order to provide a direct relationship between A_r and F_N , which is however only valid for small normal loads – i.e., for low average contact pressure $\overline{\sigma_0}$ [27], thus:

$$A_r = \frac{2}{\pi E'} \left(\frac{\pi}{\overline{\Delta_q}(\zeta)^2} \right)^{1/2} F_N \tag{5}$$

Let us assume that:

• (i) F_N is always connected to the experimental F_T via the Coulomb's law of friction involving the friction coefficient μ of the nitinol/PTFE couple only.

• (ii) Any potential stick-slip phenomenon is yet a displacement-controlled one connected to the variations of F_N during sliding of the double cross-section stent within soft catheter, as demonstrated above.

Thus, the first assumption only considers the materials component of friction whereas the second one adds the stent design influence on tribological behaviour. Hence, Eq. 5 can be replaced by Eq. 6 which is a relationship that now involves (*i*) the evolution of the friction force extracted from Fig. 11 in pulling and pushing for various sliding velocities and, (*ii*) the friction coefficient of nitinol/PTFE couple, itself experimentally assessed by tensile testing when a smooth nitinol tube is rubbing within the PTFE catheter for all defined normal loads (Fig. 12) and sliding velocities (Fig. 13), respectively.

$$A_r(d, V, \overline{\sigma_0}) = \frac{2}{\pi E'} \left(\frac{\pi}{\overline{\Delta_a}(\zeta)^2} \right)^{1/2} \frac{F_T(d, V, \overline{\sigma_0})}{\mu(d, V, \overline{\sigma_0})}$$
 (6)

Hence, Fig. 12 plots typical evolutions of both the coefficient of friction in pulling (Fig. 12a) and pushing (Fig. 12b) versus displacement assessed at $100 \,\mu\text{m.s}^{-1}$ for three normal loads imposed by the torque screw (see Fig. 4b), while Fig. 13a and Fig. 13b display same evolutions at a normal load of 8.2 N for three sliding velocities, respectively. Whatever the applied normal load or sliding velocity, friction coefficients are quite stable in traction and compression because they only take into account the materials properties of tribological couple without any influence of roughness's owing to the good surface finish of the nitinol tube($R_q = 216.7 \pm 29.8 \, \text{nm}$). As a result, the average values of friction coefficients, reported in Table 4 for various sliding velocities, correspond to the materials frictional components only.

It is worth noting that a maximum (theoretical) value of μ can be computed by using Eq. 6 and the theory of elastomer's friction [30]. It can be then used as reference allowing to estimate the smallest real contact area that could be expected. The main assumption only considers that the soft catheter perfectly matches on the stent topography, leading to $\mu_{theo} = \frac{F_T}{F_N} \approx \overline{\Delta_q}$. Comparing this friction coefficient – computed from $\overline{\Delta}_q$ assessed in §3.1.1 – with the experimental ones compiled

in Table 4, reveals that $\overline{\mu}_{exp} \approx 0.3 \cdot \mu_{theo}$, which means that the assessed experimental real contact area will be likely to be up to three times the theoretical minimum one.

By inserting experimental friction coefficients from Table 4 in Eq. 6, the evolution of the real contact area versus stent displacement in traction and compression can finally be plotted and studied in Fig. 14 for three sliding velocities by using data from Fig. 11.

As expected, the real contact area strongly fluctuates around an average value $\overline{A_r}$ compiled in Table 5 for all sliding velocities in pulling and pushing tests. As mentioned above, these fluctuations are probably linked to some *displacement-controlled stick-slip* phenomenon induced by normal force variations (or contact normal pressure) as function of the location over the sliding surface. The latter are clearly due to the non-uniform stent surface which continuously change the average contact pressure during sliding. Nevertheless, average real contact area decreases with the sliding velocity in pulling testing whereas it stays quite constant in pushing ones. In addition, it is worth noting that the fluctuation amplitudes are still in the same order of magnitude for all testings because the contact pressure variations are only controlled by the difference of contact pressure induced by the double section of the stent. Besides, whatever the test velocity, the real contact area is always lower in pushing than pulling tests decreasing, by this way, the friction reaction during the normal conditions stent release.

As a result, there is a way to reduce stick-slip phenomena induced by the presence of the both stent diameters (i.e., Leg and Body). This basically consists to reduce the standard deviation of the average actual contact area (Fig. 14) by jointly optimizing the topography of each stent part. Indeed, by combining Eq. 1 and Eq. 4, it appears that only the ratio $\frac{\Delta D}{\Delta_q}$ needs to be optimized to ensure to have the same real contact area on the both stent parts – i.e., $\frac{\Delta D^{Leg}}{\Delta_q^{Leg}} \approx \frac{\Delta D^{Boddy}}{\Delta_q^{Body}}$. Since, the design parameter ΔD cannot be easily modified because it encompasses, in particular, functional constraints and materials properties of stent, only the topographical parameter Δ_q is likely to be optimized in order to have the same real contact area all over the stent. This can be carried out by suitable surface treatments allowing to change Δ_q of each stent part, in order to compensate the jump of contact pressure $\Delta \sigma_0$ induced by the double section of the stent. It is worth noting that this topographical criterion should also enable to optimize the friction force during the stent release as it acts on the dynamic real contact area too (Eq 6). Finally, as shown in Fig. 10, the static real contact area being strongly dependent on the stent design, the latter is also likely to influence its

behaviour in dynamics.

3.3. Evolution of the tangential stress at the interface

Tangential stress τ at the interface between the PTFE catheter and nitinol stent, for an average 309 contact area ratio of 1.5 \pm 0.16 %, can finally be computed and plotted in Fig. 15 by dividing 310 the tangential force F_T (Fig. 11) by the real contact area A_r (Fig. 14) for each sliding velocity, in 31 pushing and pulling testings. Of course, this value appears to be quite high versus the mechanical 312 yield stress of PTFE but this tangential stress is only applied on 1.5% of the nomimal contact area. 313 Nevertheless, it is worth noting that this value is high enough to be responsible of the catheter 314 wear leading to freed PTFE particles during stent release, as experimentally noticed. Besides, this tangential stress is quite independent of the velocity in pushing tests, whereas it continuously 316 increases with velocity in pulling tests. Fortunately, the stent release is always carried out by 317 compression – i.e., pushing. 318 The knowledge of this evolution can finally be useful for simplifying the numerical simulations

The knowledge of this evolution can finally be useful for simplifying the numerical simulations of stent release behaviour. Indeed, its friction law is implicitly integrated in the stent design.

Therefore, the complex geometry of a stent can be then modelled by a simple tube displaying a complex frictional behaviour by distributing the computed tangential stress over a very small fraction - i.e., 1.5% in this case - of the whole contact area. In addition it is worth mentioning that any change in the stent geometry leads to alter the rigidity of its structure once compressed into the catheter and, therefore, modify the tangential stress at the interface too.

326 4. Conclusion

In this study, the frictional behaviour of a nitinol stent sliding within a PTFE catheter has been characterised using an original multi-scale approach. First, the static average real contact area has been evaluated by combining X-ray tomography, topographical analysis, and Persson's contact theory in order to determine: (*i*) the average contact pressure generated by the nitinol stent within the PTFE catheter and, (*ii*) the average contact area ratio, which completely defines the discrete static real contact area. Secondly, dynamics of the latter, in sliding induced by the stent release, have been carefully studied in combination with the Persson's contact theory by using tensile testing machine for various velocities. As a result, these evolutions take into account both the

materials and geometrical parts of the friction dissipation. These assessments finally allows us to compute an equivalent tangential stress at the interface, which will be suitable to simplify any numerical simulation of the stent sliding. Then, different stent designs can be proposed and even optimized in order to reduce friction during the sliding phase throw the catheter. A topographical optimization criterion, Δ_q , was finally proposed in order to reduce both friction and stick-slip phenomenon at the stent catheter interface.

Acknowledgment

We would like to express our gratitude to the FEMTO-ST research institute, the CNRS, and the Plan France Relance for generously funding our research, enabling us to carry out this study and bring it to completion. We also wish to acknowledge Stani Carbillet and the AMETISTE platform for granting us access to the tensile testing machine and the digital microscope, and Xavier Gabrion, and the MIFHySTO platform for helping to use the X-ray tomography equipment.



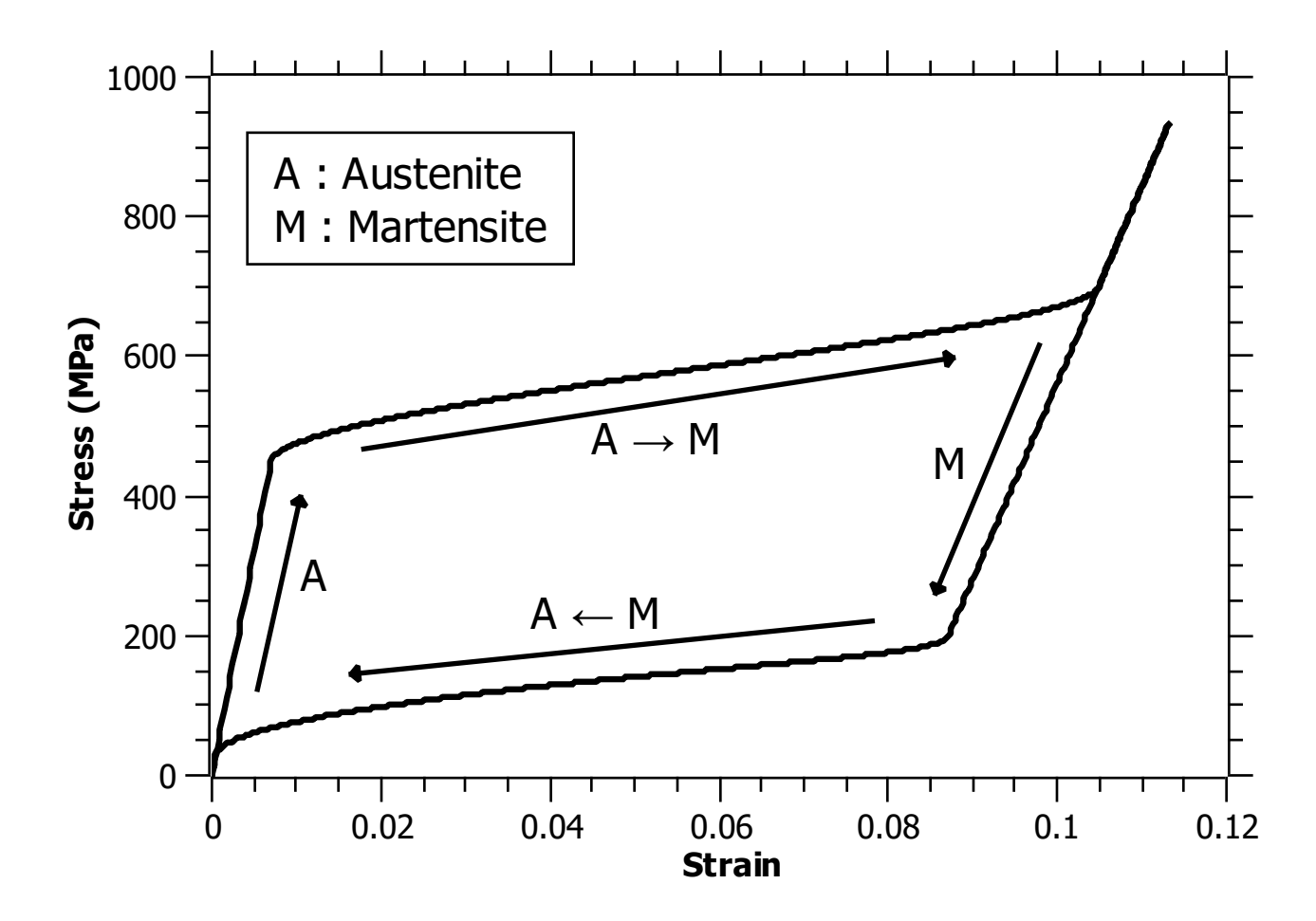


Figure 1: Typical tensile test of nitinol revealing super-elastic (SE) behaviour owing to reversible phase transformation of Austenite to Martensite

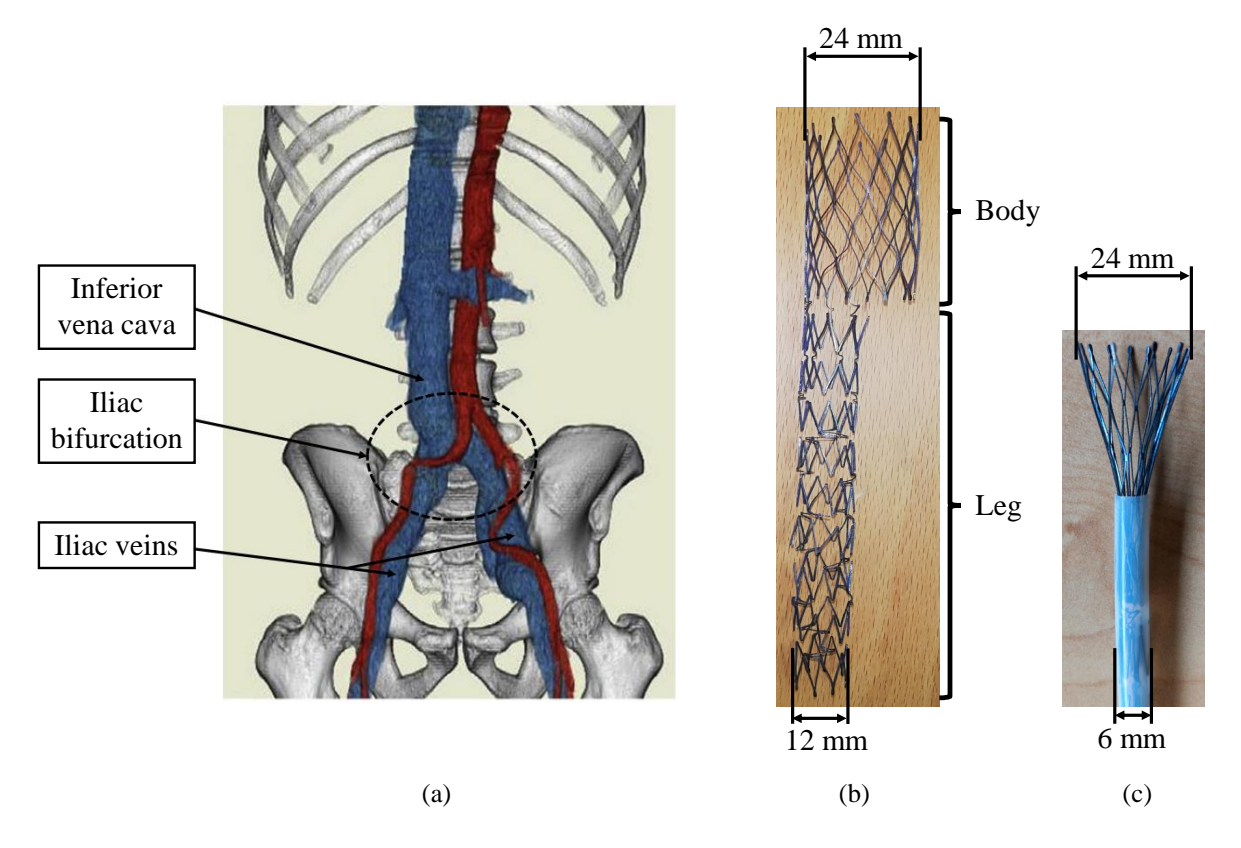


Figure 2: (a) Illustration of the inferior vena cava and the two iliac veins and the iliac bifurcation of the venous system from Onizuka et al. [31]; (b) Design of the patented one-piece double cross-sectional self-expandable stent (Leg part : ϕ : 12 mm; Body part : ϕ : 24 mm); (c) Snapshot of stent release from PTFE catheter

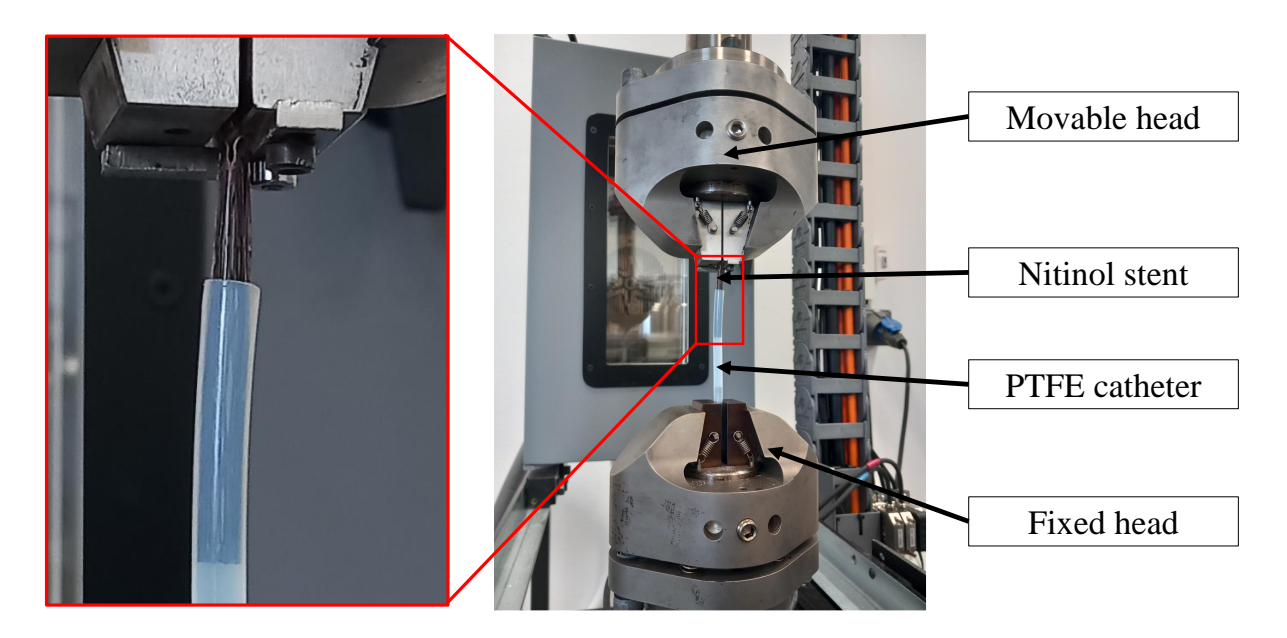


Figure 3: Tensile testing machine equipped for nitinol stent/PTFE catheter tribological test. During traction or compression the nitinol stent is pulled or pushed over 10 mm by the movable head with respect to the PTFE catheter clamped at the fixed head. The average normal pressure $\overline{\sigma_0}$ is only imposed by the radial expansion force of the nitinol stent on the PTFE catheter. The latter actually results from the both contact pressures σ_0^{Leg} and σ_0^{Body} imposed by each part of the stent compressed within the cathether, as shown in Fig 9.

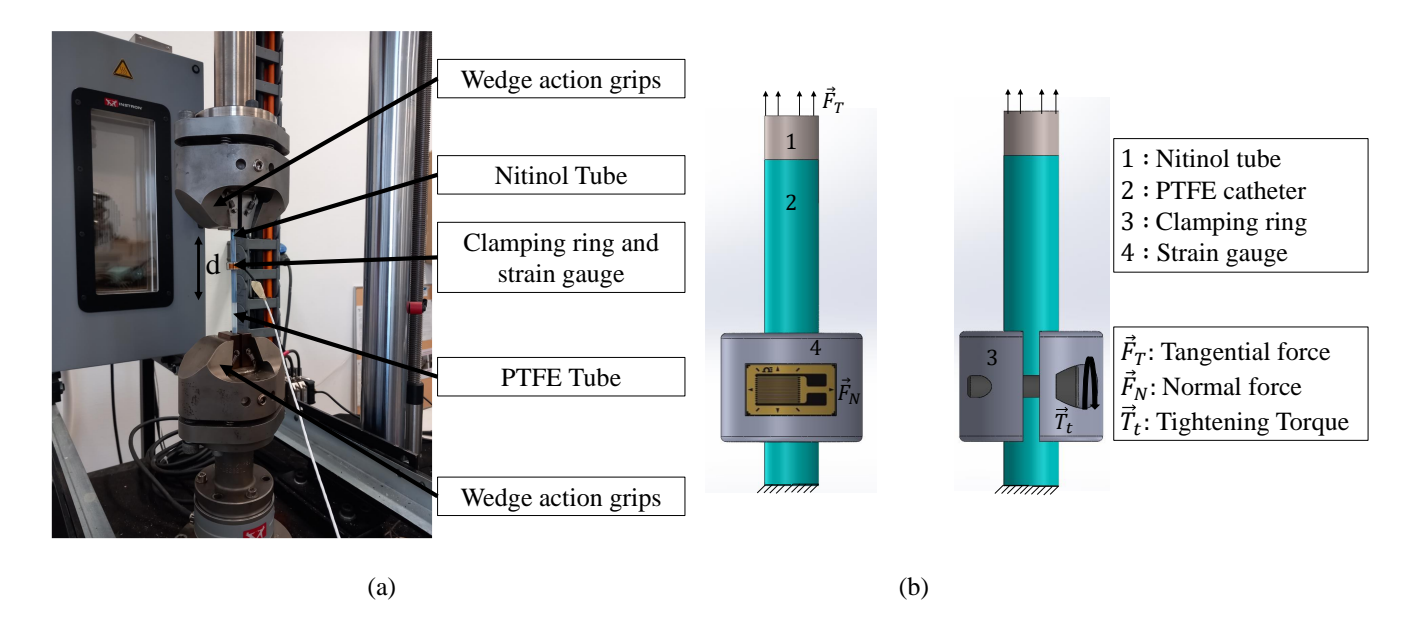


Figure 4: (a) Tensile testing machine used for nitinol tube/PTFE catheter tribological test; (b) The normal load is applied by means of a clamping ring equipped by a strain gauge. During traction or compression the nitinol tube is pulled or pushed on over 10 mm by the movable head with respect to the PTFE catheter clamped at the fixed head

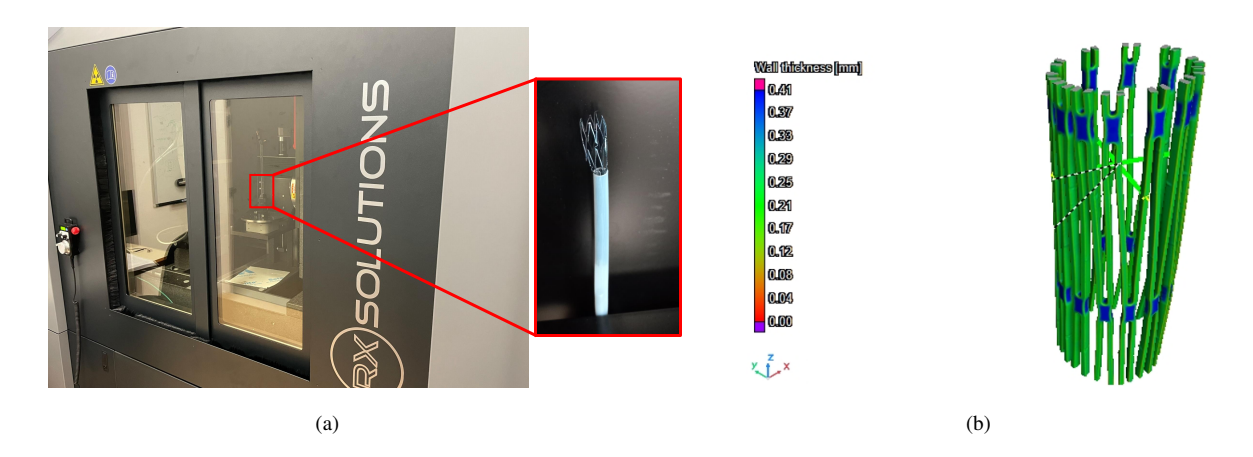


Figure 5: Tomographical analysis of nitinol stent within PTFE catheter: (a) X-ray SOLUTION EASYTOM tomographic equipment and stent/catheter assembly; (b) 3D view revealing the deformation of the nitinol stent within the PTFE catheter as reconstructed with VGstudio max software

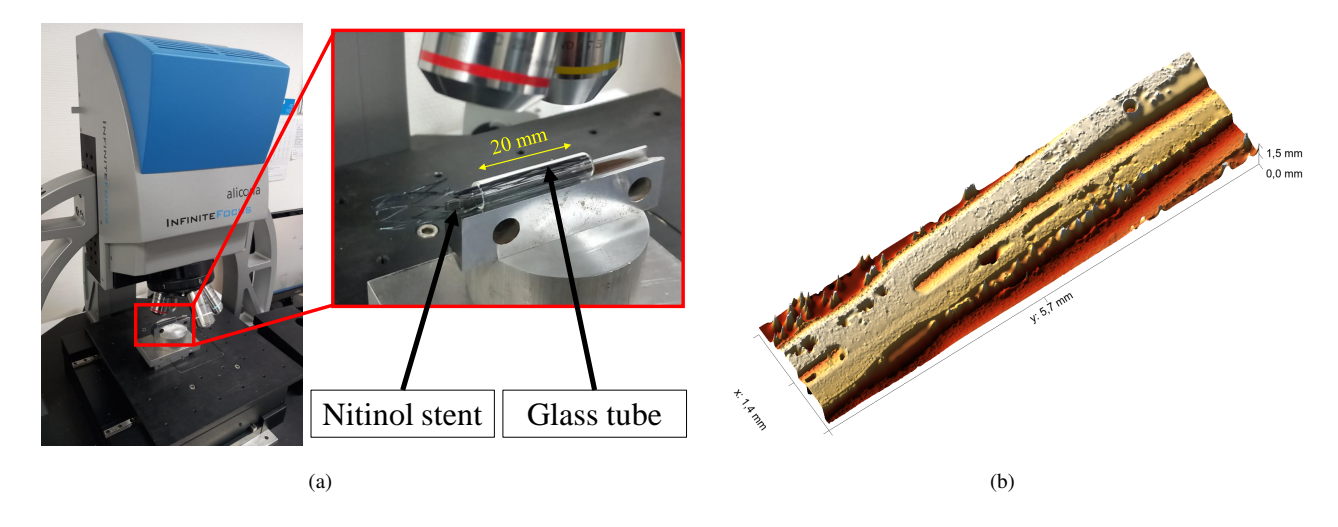


Figure 6: (a) InfiniteFocus topo-microscope ALICONA and stent/glass tube assembly enabling to characterize the stent topography compressed within the tube; (b) Typical 3D-topographical view showing various strands of the compressed stent

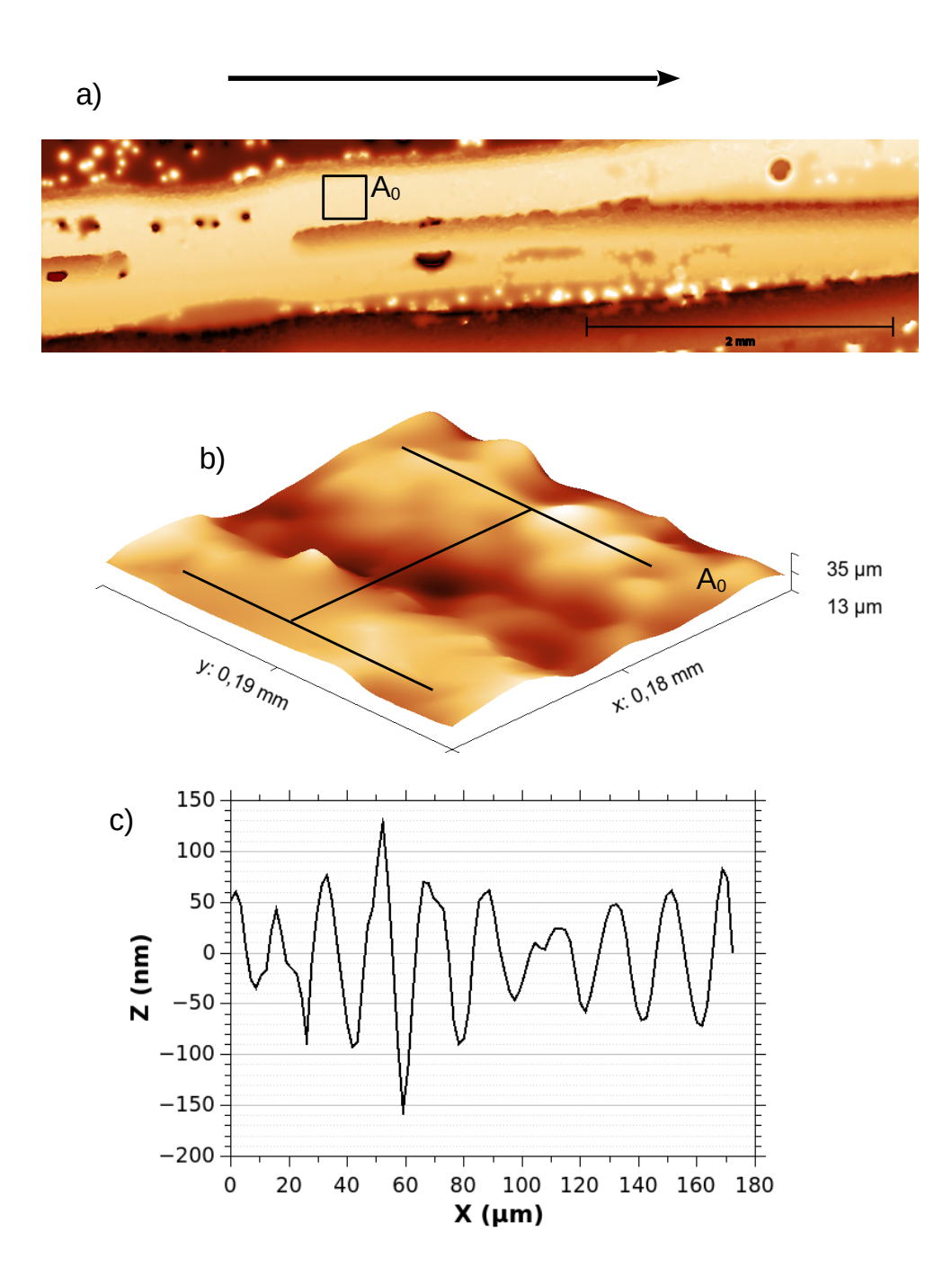


Figure 7: (a) Typical 2D-topographical view of nitinol stent within the glass tube (black arrow represents the sliding direction); (b) Enlargement of the nominal contact area A_0 extracted from Fig.7a; (c) Averaged roughness profile carried out on the whole surface picture (i.e., Fig. 7b) allowing to assess the root mean square slope $\overline{\Delta_q}$.

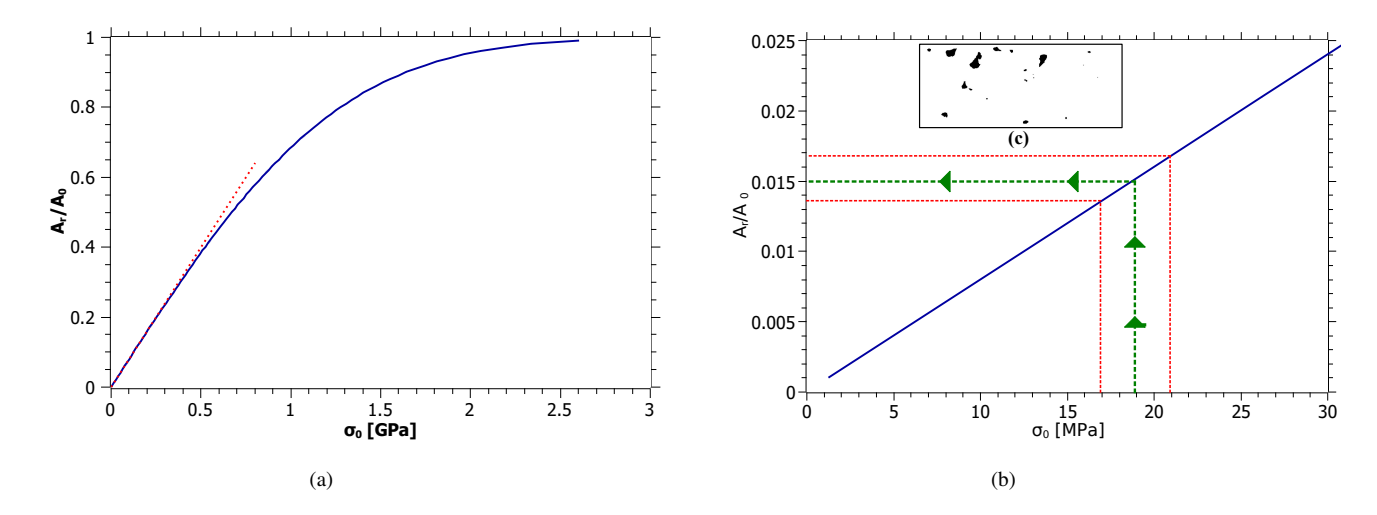


Figure 8: (a) Contact area ratio $\frac{A_r}{A_0}$ vs. contact pressure σ_0 following the Persson's contact theory; (b) Zoom in the interesting area (σ_0 = 19 \pm 2 MPa) leading to the contact area ratio of 1.5 \pm 0.16 %; (c) Experimental view of the real discrete contact area for $\frac{A_r}{A_0}$ = 1.5% corresponding to a contact pressure of σ_0 = 19 MPa

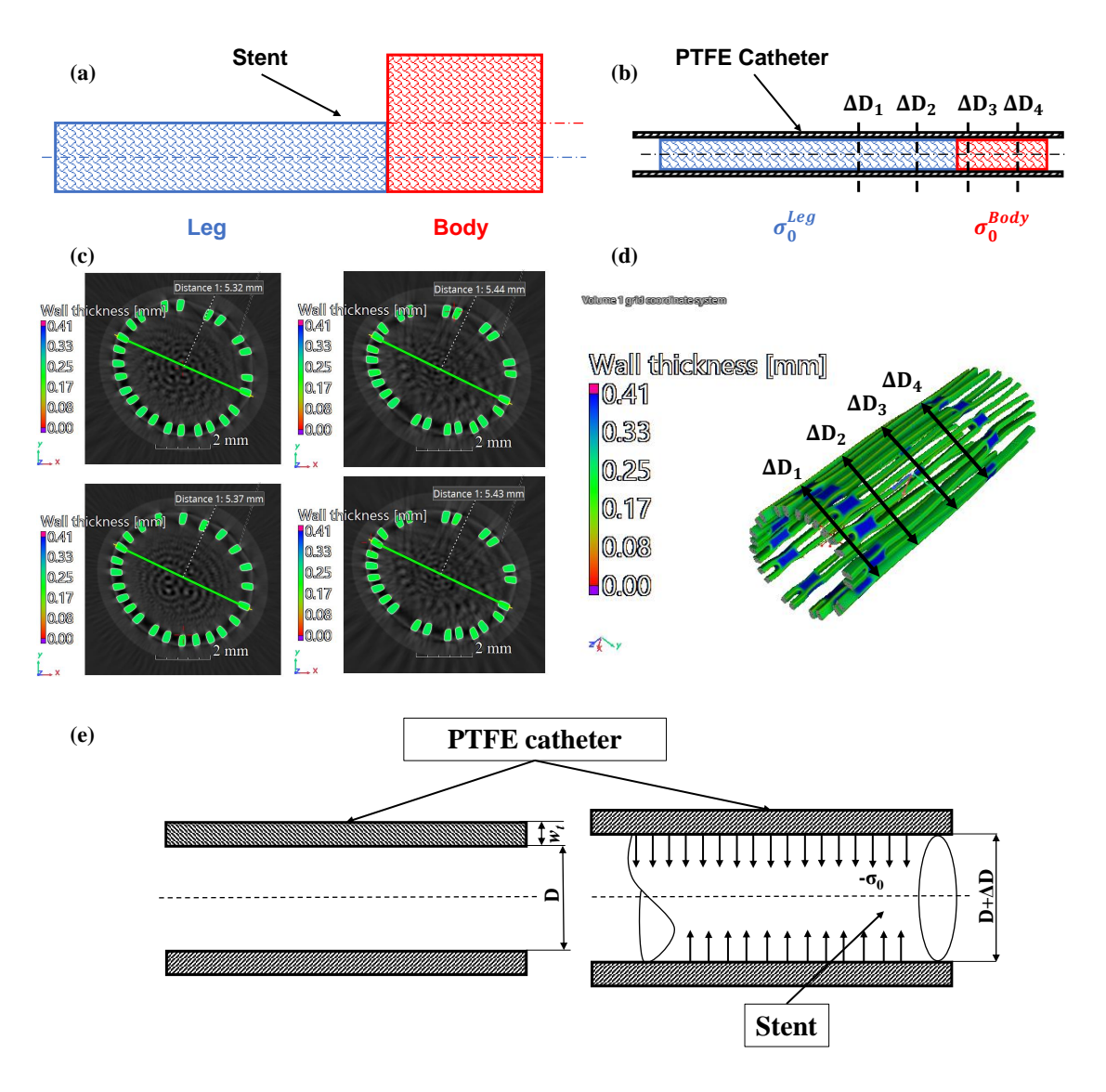
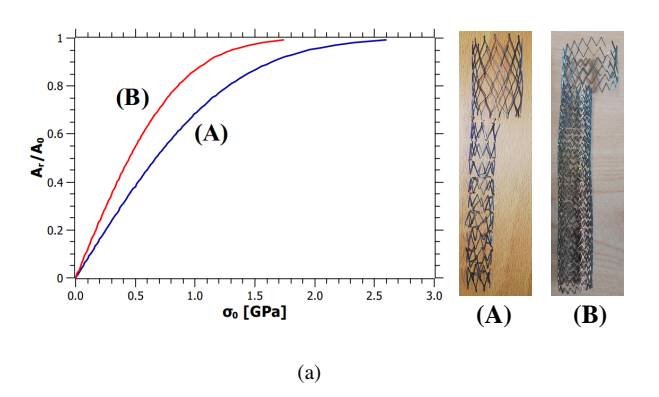


Figure 9: (a) Schematic illustration of our one-piece double cross-sectional self-expanding stent constituted by a Leg and a Body part, respectively; (b) Schematic view of the stent compressed within the PTFE catheter: each part generates a normal stress on the catheter, σ_0^{Leg} and σ_0^{Body} , leading us to only consider the average normal stress along the stent, $\overline{\sigma_0}$, that is likely to control the frictional process during the releasing. The latter is computed from catheter deformations ΔD_i assessed at different locations along the stent by using X-ray tomography; (c) Top views of the corresponding tomographical analyses revealing the deformations of the nitinol stent within the PTFE catheter at the locations pointed in Fig 9d (the average deformation $\overline{\Delta D}$ is reported in Table 2); (e) Sketch illustrating the deformation of the PTFE catheter submitted to the stent expansion and the associated parameters used in Eq. 3 and Table 2



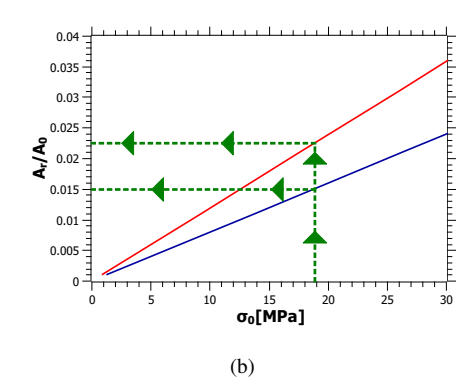
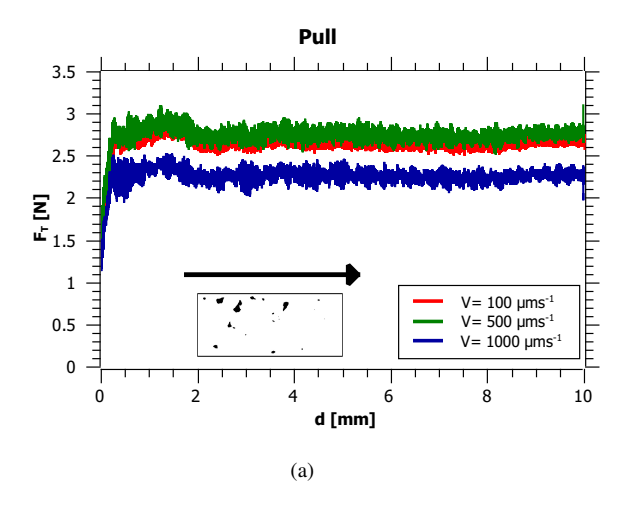


Figure 10: (a) Comparison of the contact behaviour of stents displaying two various designs – so-called (A) and (B), respectively; (b) Zoom of the curve in the interesting area ($\sigma_0 = 19$ MPa) leading to the contact area ratio of 1.5% for the current design (A) vs. 2.25% for a new design (B). Hence, changing stent design enables to optimize the real contact area for a same contact pressure, or vice versa



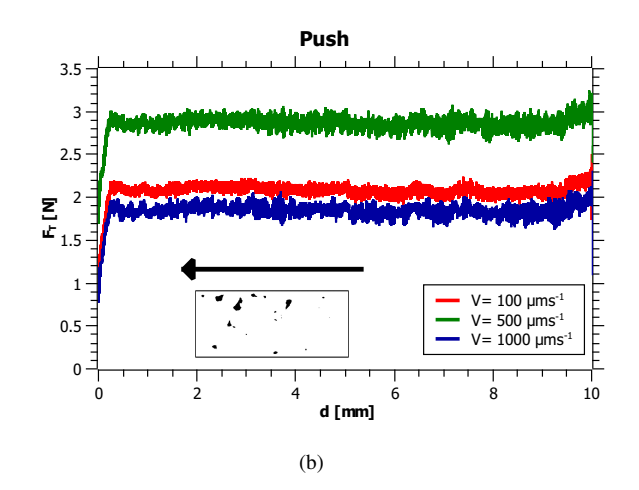


Figure 11: Evolution of the tangential force occurring between the nitinol stent (A) and the PTFE catheter *vs.* displacement in (a) traction (pull) and in (b) compression (push) for all sliding velocities (smoothed with a 20 points adjacent averaging algorithm). Insert shows the corresponding discrete real contact area and the sliding direction

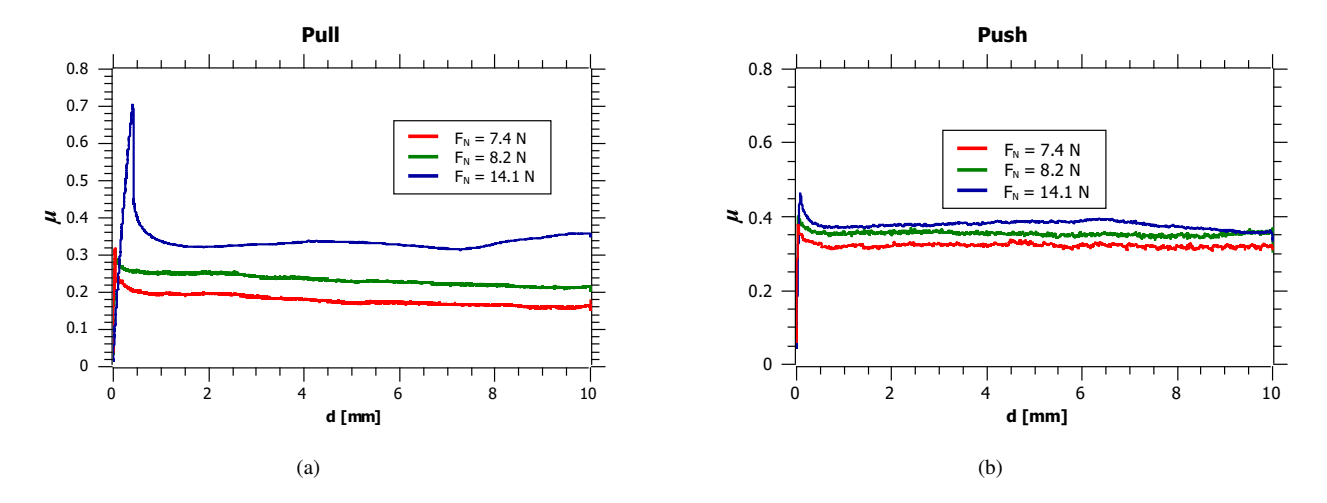


Figure 12: Evolution of friction coefficient between the nitinol tube and the PTFE catheter vs. displacement in (a) traction (pull) and in (b) compression (push) at 100 μ m.s⁻¹ for all normal loads F_N (smoothed with a 20 points adjacent averaging algorithm)

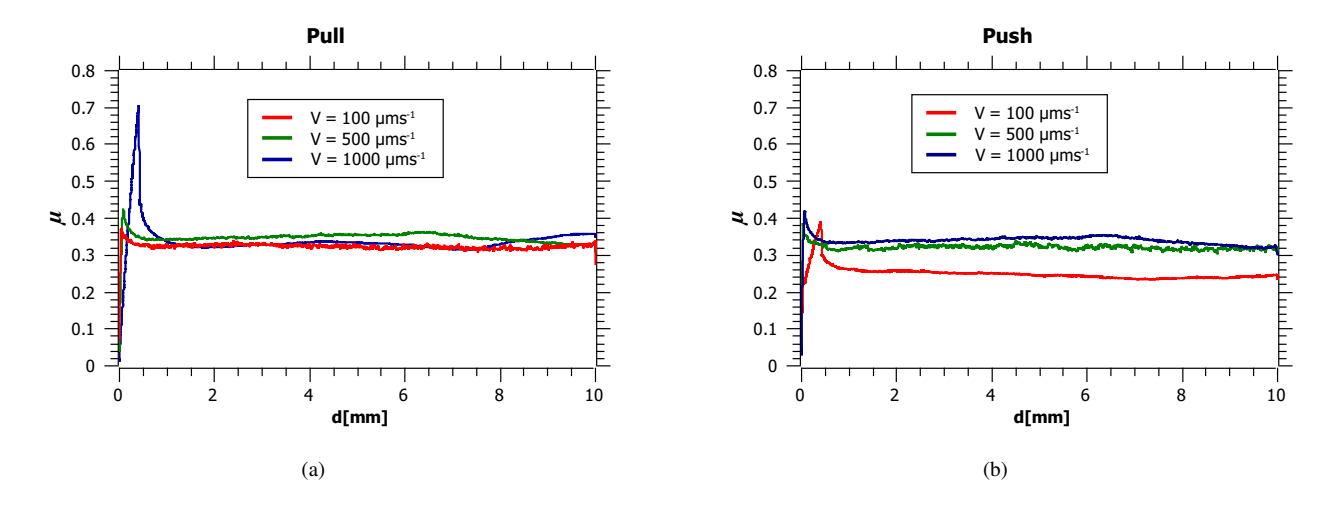


Figure 13: Evolution of friction coefficient between the nitinol tube and the PTFE catheter vs. displacement in (a) traction (pull) and in (b) compression (push) at $F_N = 8.2$ N, for all sliding velocities (smoothed with a 20 points adjacent averaging algorithm)

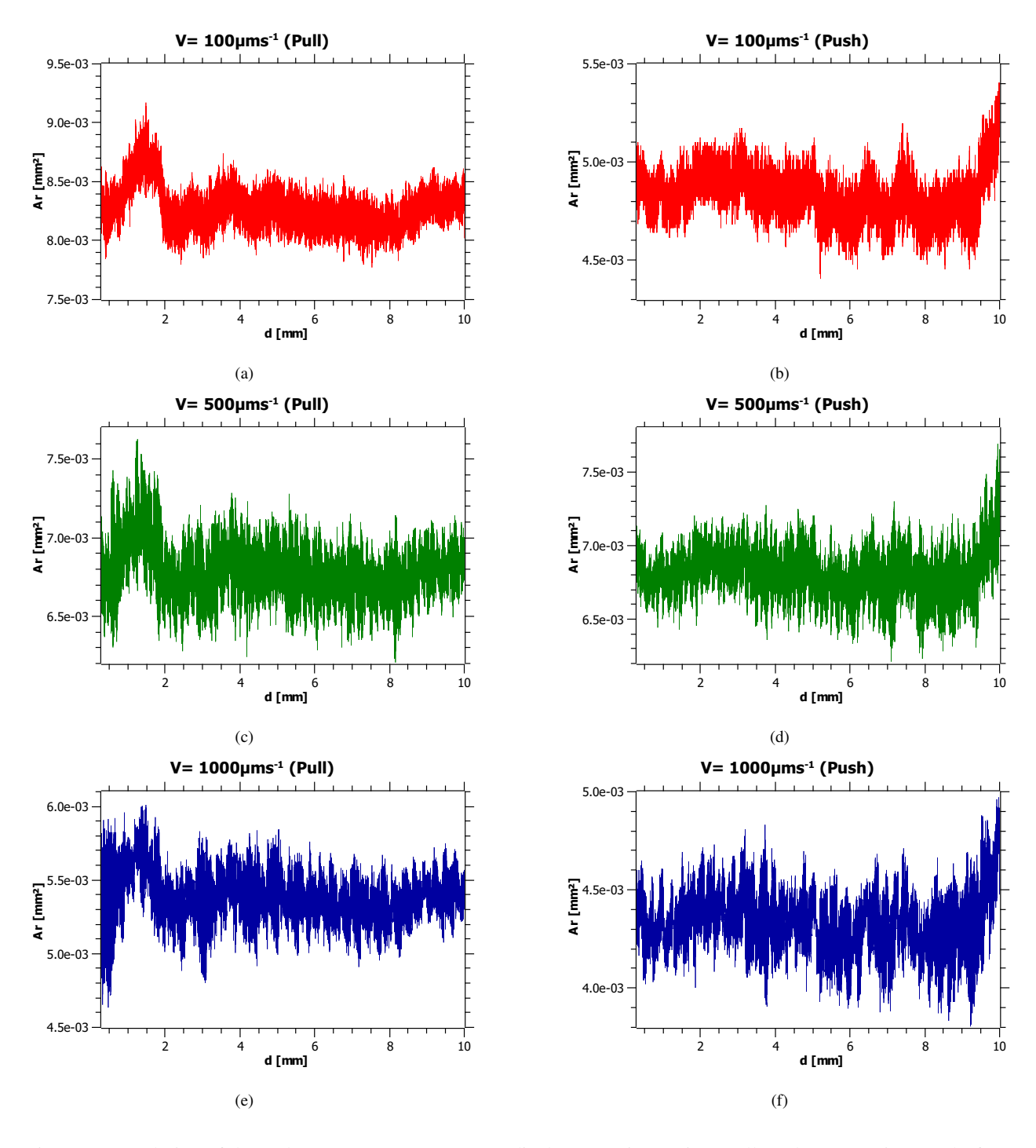


Figure 14: Evolution of the real contact area *vs.* stent (A) displacement in traction (pull) and compression (push) for different velocities

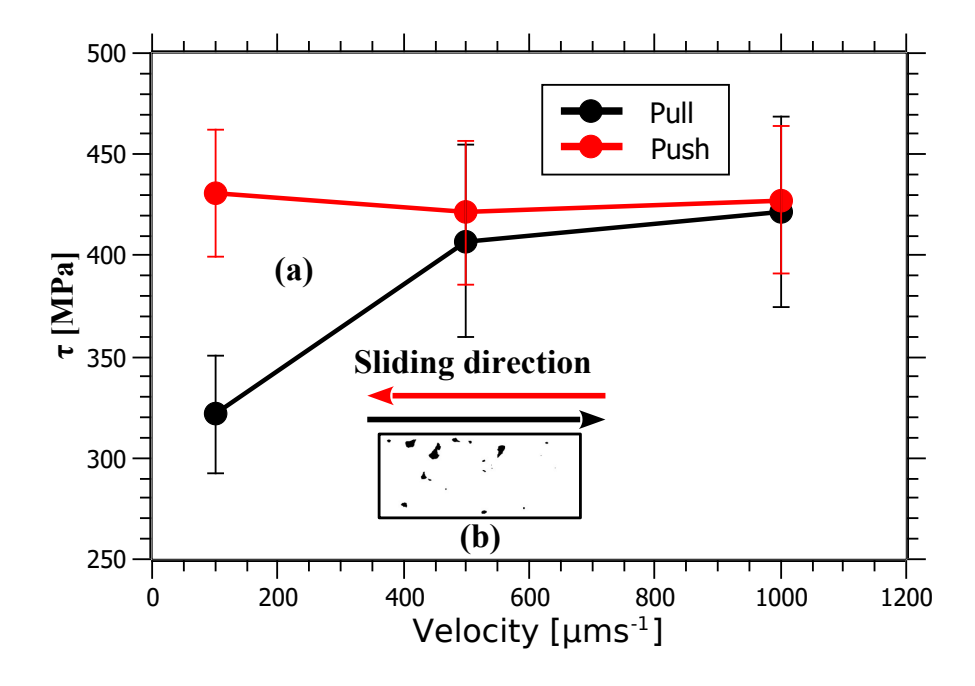


Figure 15: (a) Evolution of the tangential stress at the stent/PTFE interface vs. velocity in traction (pull) and compression (push) tests ($\frac{A_r}{A_0} = 1.5\%$, i.e., Design A); (b) insert shows the corresponding discrete real contact area and the sliding direction

	Nitinol		PTFE
	Austenite (A)	Martensite (M)	
Young's modulus E (MPa)	61540	28230	1200
Poisson's ratio v	0.33		0.46

Table 1: Mechanical properties of PTFE and different phases constituting the nitinol austenite (A) and martensite (M), respectively

Inner diameter D (mm)	5
Inner diameter deformation $\overline{\Delta D}$ (mm)	0.394 ± 0.048
Wall thickness w_t (mm)	0.5

Table 2: PTFE catheter dimensions used in Eq. 3

Velocity (μm.s ⁻¹)	Friction force F_t (N) [Pull]	Friction force F_t (N) [Push]
100	2.62 ± 0.08	2.11 ± 0.05
500	2.77 ± 0.13	2.95 ± 0.07
1000	2.35 ± 0.11	1.8 ± 0.05

Table 3: Average friction force vs. sliding velocity of stent sliding within cathether in pulling and pushing

		Sliding Velocity (μm.s ⁻¹)		
		100	500	1000
μ	Pull	0.35 ± 0.01	0.34 ± 0.01	0.34 ± 0.01
	Push	0.26 ± 0.01	0.33 ± 0.01	0.34 ± 0.01

Table 4: Mean values and standard deviations of friction coefficients of nitinol tube sliding within PTFE catheter for various sliding velocities in pulling and pushing tests

Velocity (μm.s ⁻¹)	Real contact area A_r (mm ²) [Pull]	Real contact area A_r (mm ²) [Push]
100	$8.45 \ 10^{-3} \pm 6.50 \ 10^{-4}$	$4.95\ 10^{-3}\pm 4.51\ 10^{-4}$
500	$6.97 \ 10^{-3} \pm 6.25 \ 10^{-4}$	$6.90\ 10^{-3}\pm 6.05\ 10^{-4}$
1000	$5.30\ 10^{-3}\pm5.10\ 10^{-4}$	$4.38\ 10^{-3}\pm 4.24\ 10^{-4}$

Table 5: Mean values and standard deviations of real contact area for various sliding velocities

48 References

- [1] W. J. Buehler, J. V. Gilfrich, and R. C. Wiley, "Effect of low-temperature phase changes on the mechanical properties of alloys near composition TiNi," *Journal of Applied Physics*, vol. 34, no. 5, pp. 1475–1477, 1963.
- [2] E. Farber, J.-N. Zhu, A. Popovich, and V. Popovich, "A review of niti shape memory alloy as a smart material produced by additive manufacturing," *Materials Today: Proceedings*, vol. 30, pp. 761–767, 2020.
- [3] L. Guo, F. Chen, S. Chen, Y. Huang, J. Zhang, C. Wang, and S. Yang, "The improvement of the shape memory effect of cu-13.5al—4ni high-temperature shape memory alloys through cr-, mo-, or v-alloying," *Journal of Science: Advanced Materials and Devices*, vol. 8, no. 2, p. 100532, 2023.
- ³⁵⁹ [4] D. W. Menna, A. S. Genikomsou, and M. F. Green, "Effect of heat treatment and end-hook geometry on pullout behaviour of heavily cold worked superelastic niti shape memory alloy fibres embedded in concrete," *Construction and Building Materials*, vol. 361, p. 129630, 2022.
- ³⁶³ [5] R. Bertolini, S. Bruschi, A. Ghiotti, E. Savio, L. Ceseracciu, and I. Jawahir, "Surface integrity ³⁶⁴ and superelastic response of additively manufactured nitinol after heat treatment and finish ³⁶⁵ machining," *CIRP Annals*, 2023.
- [6] D. Stoeckel, "Nitinol medical devices and implants," *Minimally invasive therapy & allied technologies*, vol. 9, no. 2, pp. 81–88, 2000.
- ³⁶⁸ [7] D. J. Hartl and D. C. Lagoudas, "Aerospace applications of shape memory alloys," *Proceedings of the Institution of Mechanical Engineers, Part G: Journal of Aerospace Engineering*, vol. 221, no. 4, pp. 535–552, 2007.
- [8] P. Xolin, C. Collard, M. Engels-Deutsch, and T. Ben Zineb, "Finite element and experimental structural analysis of endodontic rotary file made of cu-based single crystal sma considering a micromechanical behavior model," *International Journal of Solids and Structures*, vol. 221, pp. 180–196, 2021.

- ³⁷⁵ [9] D. Stoeckel, A. Pelton, and T. Duerig, "Self-expanding nitinol stents: material and design considerations," *European radiology*, vol. 14, pp. 292–301, 2004.
- [10] A. Pelton, D. Stöckel, and T. Duerig, "Medical uses of nitinol," in *Materials science forum*, vol. 327. Trans Tech Publ, 2000, pp. 63–70.
- ³⁷⁹ [11] A. Sallami, P. Malecot, F. Richard, M. Fontaine, A. Lejeune, S. David, P. Vescovo, C. Moureaux, and P. Stempflé, "The effect of heat treatment on the mechanical behavior of an ASTM-F2063 nitinol stent intended for venous application," May 2023, poster. [Online]. Available: https://hal.science/hal-04576558
- ³⁸³ [12] R. Chaudhari, J. J. Vora, and D. Parikh, "A review on applications of nitinol shape memory alloy," *Recent Advances in Mechanical Infrastructure: Proceedings of ICRAM 2020*, pp. 123–132, 2021.
- ³⁸⁶ [13] C. Cisse, W. Zaki, and T. Ben Zineb, "A review of constitutive models and modeling tech-³⁸⁷ niques for shape memory alloys," *International Journal of Plasticity*, vol. 76, pp. 244–284, ³⁸⁸ 2016.
- ³⁸⁹ [14] A. Sallami, W. Khalil, T. Bouraoui, and T. Ben Zineb, "A finite-strain thermomechanical behavior model for iron-based shape memory alloys accounting for coupling between phase transformation and plastic slip," *International Journal of Plasticity*, vol. 124, pp. 96–116, 2020.
- ³⁹³ [15] E. D. Avgerinos, Z. Saadeddin, A. N. Abou Ali, Y. Pandya, E. Hager, M. Singh, G. Al³⁹⁴ Khoury, M. S. Makaroun, and R. A. Chaer, "Outcomes and predictors of failure of iliac vein
 ³⁹⁵ stenting after catheter-directed thrombolysis for acute iliofemoral thrombosis," *Journal of*³⁹⁶ *Vascular Surgery: Venous and Lymphatic Disorders*, vol. 7, no. 2, pp. 153–161, 2019.
- ³⁹⁷ [16] S. Vad, A. Eskinazi, T. Corbett, T. McGloughlin, and J. P. Vande Geest, "Determination of Coefficient of Friction for Self-Expanding Stent-Grafts," *Journal of Biomechanical Engineering*, vol. 132, no. 12, 2010, 121007.
- [17] B. Persson, "Contact mechanics for randomly rough surfaces," *Surface Science Reports*, vol. 61, no. 4, pp. 201–227, 2006.

- ⁴⁰² [18] T. Connolley, D. Nash, J.-Y. Buffière, F. Sharif, and P. E. McHugh, "X-ray micro-tomography of a coronary stent deployed in a model artery," *Medical Engineering & Physics*, vol. 29, no. 10, pp. 1132–1141, 2007.
- [19] H. Meliani, M. Assoul, M. Fontaine, V. Malkhasyan, A. Gilbin, and G. Monteil, "Femtosecond laser–matter interaction of tungsten carbide," *Appl. Opt.*, vol. 60, no. 3, pp. 621–625,
 Jan 2021.
- [20] N. David and K. Petr, "Gwyddion: an open-source software for spm data analysis," *Open Physics*, vol. 10, no. 1, pp. 181–188, 2012.
- [21] P. Stempfle, A. Domatti, J. Takadoum, A. Fahs, and P. Carrière, "Thermal-controlled frictional behaviour of nanopatterned self-assembled monolayers as triboactive surfaces," *Tribology Letters*, vol. 68, no. 2, p. 55, 2020.
- ⁴¹³ [22] C. Li, S. Dong, and G. Zhang, "Evaluation of the root-mean-square slope of 3d surface topography," *International Journal of Machine Tools and Manufacture*, vol. 40, no. 3, pp. 445–454, 2000.
- B. Persson, F. Bucher, and B. Chiaia, "Elastic contact between randomly rough surfaces: comparison of theory with numerical results," *Physical review B*, vol. 65, no. 18, p. 184106, 2002.
- ⁴¹⁹ [24] J. A. Greenwood and J. P. Williamson, "Contact of nominally flat surfaces," *Proceedings*⁴²⁰ of the royal society of London. Series A. Mathematical and physical sciences, vol. 295, no.
 ⁴²¹ 1442, pp. 300–319, 1966.
- ⁴²² [25] A. Bush, R. Gibson, and T. Thomas, "The elastic contact of a rough surface," *Wear*, vol. 35, no. 1, pp. 87–111, 1975.
- ⁴²⁴ [26] P. Stempflé and N. Ratier, "What does a sliding triboelectrical sensor really measure?" *Tri-*⁴²⁵ *bology International*, vol. 179, p. 108083, 2023.
- ⁴²⁶ [27] G. Carbone and F. Bottiglione, "Asperity contact theories: Do they predict linearity between contact area and load?" *Journal of the Mechanics and Physics of Solids*, vol. 56, no. 8, pp. 2555–2572, 2008.

- [28] F. Esnault, *Ingénierie mécanique: Tome 3*. Paris: DUNOD, 2019.
- [29] C. M. Mate, *Tribology on the small scale: a bottom up approach to friction, lubrication, and*wear. Oxford university press, USA, 2007.
- [30] V. Popov, Contact Mechanics and Friction. Springer, 2017.
- H. Onizuka, E. Sueyoshi, I. Sakamoto, and T. Miura, "Dilation of inferior vena cava and iliac veins in elite athlete," *Journal of Vascular Surgery: Venous and Lymphatic Disorders*, vol. 5, p. 575, 2017.